Sensors and Materials, Vol. 34, No. 6 (2022) 2141–2153
MYU Tokyo

S & M 2961

Design of Automatic Test System for Dynamic Performance of Magnetic Head Based on Machine Vision

Long Gao,[1] Jian-Yong Bian,[1*] and Feng-Peng Wang[2]

[1]School of Electronic Information, DongGuan Polytechnic, DongGuan 523000, China
[2]Testing Engineering Division, XinKe Magnetoelectric Co. Ltd., DongGuan 523000, China

(Received December 6, 2021; accepted April 20, 2022)

Keywords: magnetic head, machine vision, automatic test, hand-eye calibration, CCD image sensor

The dynamic performance test of a hard disk head is the most effective method of evaluating hard disk performance, but it must be conducted in a dust- and electrostatic discharge (ESD)-free environment. With the rapid development of perpendicular magnetic recording (PMR) technology, the flying height of a magnetic head is reduced from 18 nm to less than 2 nm, which makes the testing conditions increasingly demanding, and the traditional way of manual testing by an operator cannot match the requirement of production testing. To meet the technical requirement of the dynamic performance test of a hard disk head, an automatic test system is developed using a CCD image sensor and an Epson robot. In this system, the vision system of the robot can accomplish, in real time and accurately, the image acquisition and image processing of the object in the magnetic head testing process and calculate the actual position of the object after hand–eye calibration. Visual guidance is provided to the robot to grasp and place the target accurately, and related sensors provide various state data during the system operation. Thus, the difficult problem in the development process from manual operation to robot automation in the dynamic performance test of a magnetic head is successfully solved. The results show that the consumption of test materials is considerably reduced, and the test precision and efficiency are markedly improved.

1. Introduction

The dynamic performance test of a magnetic head can yield the parameters closest to those of the operation of the hard disk. The testing includes three stages, namely, magnetic core loading, magnetic head transfer, and dynamic performance testing. At present, the entire testing process is mainly conducted manually by operators, which affects production efficiency and product reliability. At the same time, under the pressure of increasing labor costs in recent years, major hard disk head manufacturers and suppliers must research and develop advanced automation systems to replace operators to ensure their company's competitive advantage.

CCD image sensors and machine vision are studied and used widely. Sun *et al.* designed an application-specific integrated circuit (ASIC) for CCDs.(1) Stevens *et al.* described recent process modifications made to enhance the performance of interline and electron-multiplying CCD

*Corresponding author: e-mail: Bianjy@dgpt.edu.cn
https://doi.org/10.18494/SAM3800

ISSN 0914-4935

(EMCCD) image sensors.[2] Dwivedi *et al.* evaluated the percentage error in the measurement of length, distance, and angle using the CCD pixel counting technique.[3] Astier certified static image distortions on deep-depleted CCD sensors and presented a summary of the results of CCD sensor characterization and mitigation methods.[4] Xia *et al.* proposed that, compared with traditional industrial sensor signals, machine vision systems can quickly understand manufacturing scenarios and provide the extracted semantic information to manufacturing ontologies developed by experts or ML-enabled network systems.[5] Leary used machine vision technology to monitor the entire metal rolling process and realized visual feedback control of the entire system through a high-speed data transmission network.[6] Benjamin *et al.* used a machine vision system to measure the morphological features of Radiata pine seedling.[7] Kim *et al.* applied machine vision to detect steel frame damage and effectively facilitated the real-time inspection and location of steel frame damage.[8] Bouguettayaa *et al.* focused on the detection of wildfires at their early stages in forest and wildland areas, using deep-learning-based computer vision algorithms to prevent wildfires.[9] Chian *et al.* applied machine vision for detecting missing barricades.[10] Hashemzadeh and Farajzadeh developed a fertility detection machine vision system that is highly reliable and applicable in the incubation industry.[11] Niu designed a defect detection system for semiconductor plastic packaging based on machine vision.[12] Yang discussed the design of industrial robots using machine vision and deep learning, providing a reference for the combination of deep learning and machine vision and industrial robots.[13] Eshkevari *et al.* developed a machine vision system for measuring and controlling the dimensional characteristics of medical glass vials.[14]

In this study, we developed a set of automated testing systems suitable for a dust-free production environment. For the first time, industrial robots, CCD image sensors, and machine vision technology were applied to the dynamic performance test of hard disk magnetic heads, realizing the high-precision positioning of the target during the test.

2. Test System Model

A vision system is added to the Epson E2S551C (suitable for clean room standards) industrial robot, making it a visual industrial robot system. The whole system includes the following: Epson E2S551C robotic arm, RC420 robot controller, Sony CCD camera, and Meteoi-II PCI digital image capture card. Moreover, some peripheral monitoring sensors such as photoelectric sensors and infrared sensors are used as auxiliaries to ensure the safety of equipment and personnel. At present, cameras are usually installed in robots and vision systems in two ways.[11] The two methods are divided in accordance with the different installation positions of the camera. One way is to install the camera on the upper bracket of the robot's activity space or on a dust-free table, which is called fixed installation. The other way is to install the camera on the end-effector of the robot's arm, which is called hand–eye installation. In the fixed installation, a photograph is taken of the upper surface of the entire test platform. In the hand-eye installation, a photograph is taken of only the upper surface of the target that needs to be captured or placed at the time. In the actual measurement environment, this system uses a monocular stereo imaging system to fix the CCD camera on the end-effector of the Epson

industrial robot, and then the CCD camera moves with the industrial robot hand and collects the two-dimensional image of the target at different positions. Owing to the influence of the external environment, such as the light source, the original image contains much noise and interference. Thus, the original image needs to be smoothed by filtering, transformation, and other means, which can improve the quality of the image and enable significant edge features to be obtained. After hand–eye calibration, the robot can achieve high-precision positioning of the target. The details of its structure are shown in Fig. 1.

3. Image Processing

3.1 Grayscale transformation

During imaging, owing to factors such as uneven illumination, under- or overexposure of the image, and nonlinearity of the imaging equipment, the resulting image has insufficient contrast, which makes the image details unclear. However, through image grayscale expansion, the subjective quality of the image can be improved significantly. Assuming that the grayscale of the original image is [a, b] and the expected grayscale of the transformed image $g(x, y)$ can be expanded to [c, d], Eq. (1) can be used to achieve the linear transformation.

$$g(x,y)=\begin{cases} c & 0 \le f(x,y) \le a \\ \dfrac{d-c}{b-a}[f(x,y)-a]+c & a \le f(x,y) \le b \\ d & b < f(x,y) \le M \end{cases} \tag{1}$$

Here, M is the maximum grayscale of the image.

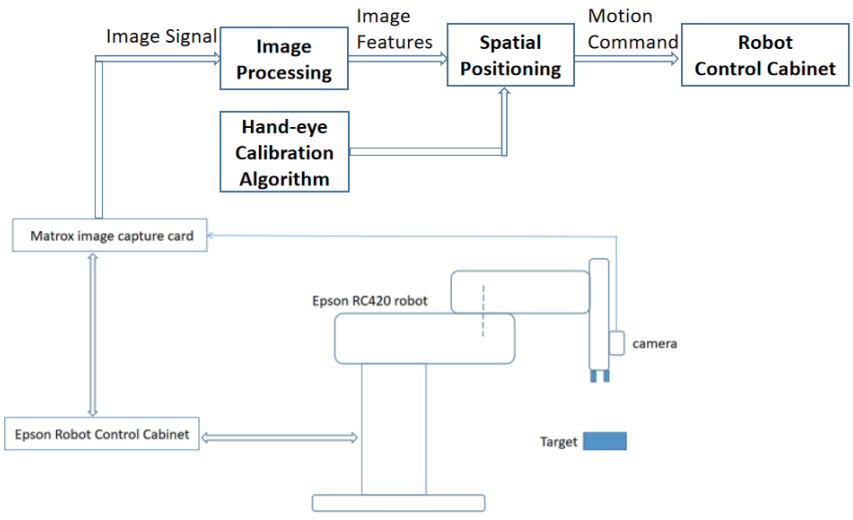

Fig. 1. (Color online) Test system architecture.

Sometimes, to highlight the target of interest or grayscale interval and suppress those grayscale areas that are not of interest, at the expense of other grayscale details, the piecewise linear grayscale method can be used to stretch the grayscale of the required image detail and compress the unwanted grayscale. Its mathematical expression is as follows.

$$g(x,y)=\begin{cases}\dfrac{c}{a}f\left(x,y\right) & 0\le f(x,y)\le a\\ \dfrac{d-c}{b-a}[f(x,y)-a]+c & a\le f(x,y)\le b\\ \dfrac{f-d}{e-b}[f(x,y)-b]+d & b\le f(x,y)\le e\end{cases} \tag{2}$$

The original image of the target used in this study is shown in Fig. 2. The image after piecewise linear transformation is shown in Fig. 3, which shows that the contrast was enhanced significantly.

3.2 Image smoothing

Because of elements such as factory electromagnetic waves and jitter noise generated by the reciprocating motion of the robot, various types of noise are generated during the image generation and transmission process. At this time, the image must be smoothed.[15] Image smoothing often uses low-pass filtering to block noise signals belonging to the high-frequency range. However, image edge information is also high-frequency information, and the smoothing process will cause edges to become blurred. During the development of our system, mean filtering and median filtering were used to smooth the target image. To maximize the preservation of the edge features of the image, after numerous experiments, the median filter technology was selected for use.

Median filtering is a nonlinear filtering technique that replaces the value of a point in a digital image or digital sequence with the median value of each point in the neighborhood of the point. For a one-dimensional signal, we assume that there is a sequence $f_1, f_2, \cdots, f_n$, taking an odd number m as the window length, and we perform median filtering on this sequence, that is, we extract m numbers from the input sequence $f_{i-v}, \cdots, f_{i-1}, f_i, f_{i+1}, \cdots, f_{i+v}$ successively, where

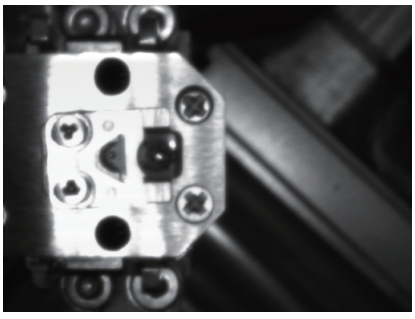

Fig. 2. Original image.

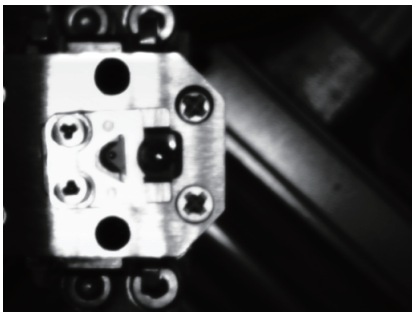

Fig. 3. Image after transformation.

$v = (m - 1) / 2$ and f_i is the center value of the window. Then, we arrange the values of the m points in the order of their numerical values and take the median value as the filtered output. The expression for median filtering is as follows.

$$y_i = \mathrm{Med}\left|f_{i-v}, \cdots, f_i, \cdots, f_{i+v}\right| \qquad i \in Z,\ v = (m-1)/2 \tag{3}$$

The median filtering of digital images is actually the median filtering of the two-dimensional sequence $\{f_{ij}\}$. The two-dimensional median filter can be expressed as below.

$$y_{ij} = \underset{A}{\mathrm{Med}}\left\{f_{ij}\right\} \tag{4}$$

Here, A is the fitering window. In actual use, we first try to use a window of length 3 to process the signal and then we extend the window length gradually until there is a better noise filtering effect with the image details being minimally damaged.

We perform median and mean filtering on the workpiece image shown in Fig. 2, and the results are shown in Figs. 4–7. A comparison shows that the mean filter has a good effect on removing random noise such as Gaussian noise, but the image boundary becomes blurred. The median filter can basically keep the boundary unchanged on the basis of filtering noise, but the template size should not be too large. The 3 × 3 template median filter effect is better than the 5 × 5 template median filter effect. Therefore, in this study, we chose 3 × 3 template median filtering.

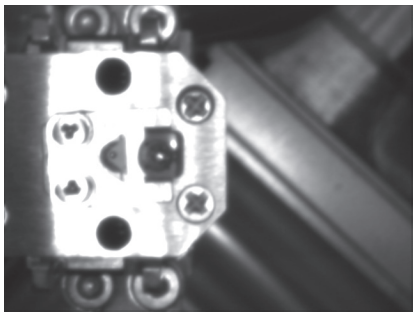

Fig. 4. 3 × 3 mean filter image.

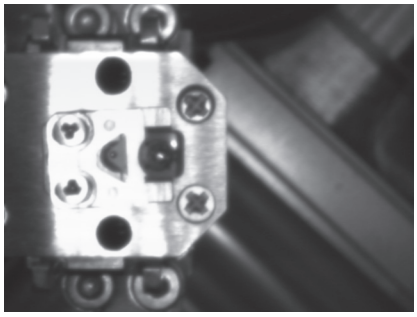

Fig. 5. 5 × 5 mean filter image.

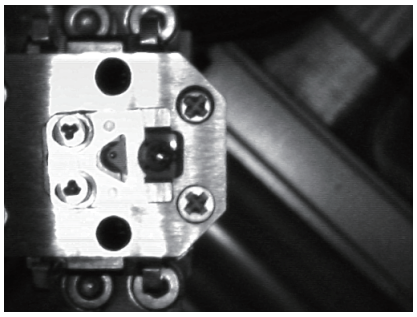

Fig. 6. 3 × 3 median filter image.

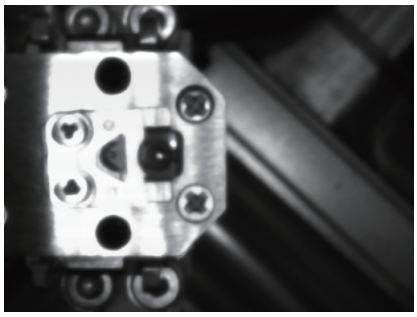

Fig. 7. 5 × 5 median filter image.

3.3 Edge feature detection

The edge is the most important feature in the image. The edges in an image can be approximated by many short straight-line segments, and each edge element is determined by a position and an angle. Commonly used edge detection operators include the Robert operator, Sobel operator, and Laplacian operator, each of which has advantages and disadvantages.[16] In this study, the internal grayscale of the target's image is relatively uniform because the image is taken at a particular application site, so the classic edge detection algorithm can meet the requirements of the desired task.

The Robert operator uses the local difference operator to find the edge, and it has a good effect on the edge detection of the image with steep and low noise. Its mathematical expression is

$$G(i,j) = |f(i,j) - f(i+1,j+1)| + |f(i+1,j) - f(i,j+1)|. \tag{5}$$

With the convolution template to express the method, the above formula becomes

$$G(i,j) = |G_x| + |G_v|. \tag{6}$$

Here, G_x and G_v are calculated using the following template.

$$G_x = \begin{bmatrix} 1 & 0 \\ 0 & -1 \end{bmatrix} \quad G_y = \begin{bmatrix} 0 & -1 \\ 1 & 0 \end{bmatrix} \tag{7}$$

The Sobel operator can handle images with more gray gradients and noises very well. The principle is to examine the weighted difference of the gray levels of the upper, lower, left, and right eight neighboring points for each pixel of the digital image $f(i, j)$. Among them, four-neighboring points can be set to have the largest weight. We define the Sobel operator as

$$\begin{aligned} S(i,j) = {} & |f(i-1,j-1) + 2f(i-1,j) + f(i-1,j+1) - f(i+1,j-1) - 2f(i+1,j) - f(i+1,j+1)| \\ & + |f(i-1,j-1) + 2f(i,j-1) + f(i+1,j-1) - f(i-1,j+1) - 2f(i,j+1) - f(i+1,j+1)|. \end{aligned} \tag{8}$$

The Log operator is implemented on the basis of the Laplacian operator shown as Eq. (9). It first uses the Gaussian low-pass filter to preslide the image, then it uses the Laplacian operator to detect the edges, and finally, the zero grayscale is used to perform binarization. This results in closed and connected contours and the elimination of all internal points.

$$\nabla^2 f(i,j) = \sum_{u,v \in S} [f(u,v) - f(i,j)] \tag{9}$$

Here, S is the set of neighboring points centered at $f(i, j)$. In the digital images, the Laplacian operator can be realized with the help of various templates. The basic requirements for the

template here are that the coefficient corresponding to the center pixel should be negative, the coefficient corresponding to the neighboring pixels of the center pixel should be positive, and their sum should be zero. The two commonly used templates are as follows.

$$G_x = \begin{bmatrix} 0 & 1 & 0 \\ 1 & -4 & 1 \\ 0 & 1 & 0 \end{bmatrix} \quad G_y = \begin{bmatrix} 1 & 4 & 1 \\ 4 & -20 & 4 \\ 1 & 4 & 1 \end{bmatrix} \tag{10}$$

We use the Robert operator, Sobel operator, and Log operator to perform edge detection on the workpiece shown in Fig. 2, and the results are shown in Fig. 8. It can be seen that the Sobel operator edge detection result has a better effect on removing shadows, but it is sensitive to noise, so there are more false edges and broken lines on the edges. The Log operator is more sensitive to noise and has more edge responses. In contrast, the Robert operator detects the edges of the target image more continuously, and the response to the edge is singular. On the basis of a comparison of the detection results of the three operators, we select the Robert operator to detect edges.

4. Hand–Eye Calibration of Visual System

In the machine vision system, when the manipulator performs a task, it is necessary to know the position of the object relative to the manipulator platform. The hand–eye calibration of the robot determines the relative position between the camera coordinate system and the end of the manipulator. To simplify the camera calibration process, the method of calculating the target position directly from the image coordinates is adopted. The method of the constant rotation matrix realizes the stereo location of the target in a specific environment on the basis of the idea of a "black box" that maps the image coordinates directly to the reference coordinates and does not demarcate the inner and outer parameters of the camera. The camera imaging process involves transformation between several different coordinate systems including the pixel coordinates *ouv*, the imaging plane coordinates *oxy*, the camera coordinates $o_c x_c y_c z_c$, and the world coordinates $O_w X_w Y_w Z_w$.[17–20] The model of each coordinate system is shown in Fig. 9.

(a) (b) (c)

Fig. 8. Edge detection using (a) Robert operator, (b) Sobel operator, and (c) Log operator.

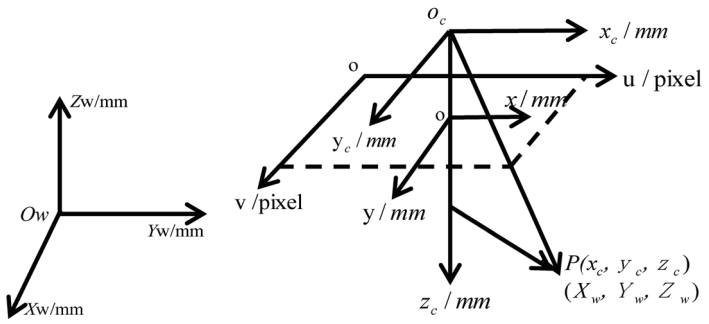

Fig. 9. Coordinate models.

If S_c is a point in the camera coordinate system and its corresponding point is S_t in the robot's outer arm coordinate system, then the camera coordinate system is transformed to the outer arm coordinate system as

$$S_t = \begin{bmatrix} R_C & P_C \\ 0 & 1 \end{bmatrix} \times S_C \cdot \tag{11}$$

$R_c \in R_{3\times3}$ is the transformation matrix from the camera coordinate system to the outer arm coordinate system, and P_c is the coordinate of the camera origin in the outer arm coordinate system. Because the camera is mounted on the robot's outer arm in this system, R_c and P_c are constant values.

If S_t is a point in the outer arm coordinate system and its mapping point is S_{oxyz} in the robot base coordinate system, then the following transformation relations exist.

$$S_{oxyz} = \begin{bmatrix} R_t & P_o \\ 0 & 1 \end{bmatrix} \times S_t \tag{12}$$

R_t is the transformation matrix from the outer arm coordinate system to the base coordinate system of the robot and is determined by the attitude of the outer arm and is independent of the position of the outer arm. P_o is the 3D coordinate value of the origin of the outer arm coordinates in the robot base coordinate system. Replacing Eq. (11) with Eq. (12) results in

$$S_{oxyz} = \begin{bmatrix} R_t & P_o \\ 0 & 1 \end{bmatrix} \times \begin{bmatrix} R_C & P_C \\ 0 & 1 \end{bmatrix} \times S_C \,. \tag{13}$$

As $f / S_{cz} = us_u / S_{cx}$ and $f / S_{cz} = vs_v / S_{cy}$, we let $f^{-1} = 1/f$, $\eta = \begin{bmatrix} s_u & 0 & 0 \\ 0 & s_v & 0 \\ 0 & 0 & 1 \end{bmatrix}$

Equation (13) can be written as

$$S_{oxyz} = R_t R_c f^{-1} S_{cz} \eta[(u, v, f)^T] + R_t R_c + P_0 \,. \tag{14}$$

If R_t in Eq. (14) is constant during system calibration, then Eq. (14) is written as

$$S_{oxyz} = S_{cz}\left\{H\left[u,v\right]^T + N\right\} + W + P_0. \tag{15}$$

Here, $H = [H_1, H_2]$ where H_1 and H_2 are the values of the first and second terms of $R_t R_c f^{-1}\eta$. N is f multiplied by the value of the third term of $R_t R_c f^{-1}\eta$, and $W = R_t P_c$. Under the above assumptions, H, N, and W remain unchanged in the calibration process. Since the system has a special photoelectric sensor on the terminal actuator to detect the height of the target, S_{cz} is constant during the calibration process. Thus, a three-dimensional problem is considered as a two-dimensional problem. Equation (15) is rewritten as

$$S_{oxy} = A\{u,v\}^T + B + P_0, \tag{16}$$

where $A = S_z \times H$ and $B = S_{cz} \times N + W$.

During the image processing of the vision system, the posture of the outer arm in the basic coordinate system of the robot remains unchanged. In Eq. (16), $\left[u,v\right]$ is calculated from the image obtained by the camera, and P_o is read directly from the robot's demonstrator. In theory, by moving the robot's end-effector to three different positions, we can obtain

$$S_{oxy} = A \times \left[u_1, v_1\right]^T + B + P_0^1 = A \times \left[u_2, v_2\right]^T + B + P_0^2 = A \times \left[u_3, v_3\right]^T + B + P_0^3. \tag{17}$$

We transform Eq. (17) to obtain

$$A([u_1, v_1]^T - [u_2 - v_2]^T) = P_0^2 - P_0^1, \tag{18}$$

$$A([u_2, v_2]^T - [u_3 - v_3]^T) = P_0^3 - P_0^2. \tag{19}$$

From Eqs. (18) and (19), we obtain

$$A * \Delta u_z = \Delta P_Z. \tag{20}$$

Δu_Z can be obtained directly from the result of image recognition, and ΔP_Z can be obtained from the robot. To reduce the error, we can move the end-effector to N positions and obtain the optimal solution A by using least squares, and then calculate B. To obtain the A and B parameter matrices, the target workpiece is taken as the calibration reference object, and the grayscale centroid of the surface of the workpiece is used as the target point of the image. In the calibration process, the CCD light source and focal length should be adjusted first to ensure that the image taken has the best quality at a specific height. In the experiment, we take the rotation matrix of the robot's pose at (−369.994, 90.062, −39.554, 136.867), and then calculate matrixes A and B.

$$A = \begin{bmatrix} -0.02257 & -0.02385 \\ -0.02368 & 0.02246 \end{bmatrix} \quad B = \begin{bmatrix} 61.100 \\ -6.078 \end{bmatrix} \tag{21}$$

During verification, placing the workpiece at the coordinates (−320.8, 84.08, −68, 0) and keeping the height and angle of the end-effector unchanged, we move the end-effector to 12 different positions to obtain 12 centroid pixel coordinates of the workpiece. Then, we calculate X and Y coordinates with the above matrix; the results are shown in Table 1. It can be seen from the table that the error between the measured value and the real value is within 0.08 mm, which can satisfy the requirements of the robot's grasping and placing tasks in the magnetic head test. To verify the repeatability, we take 50 consecutive photographs of two workpieces in different positions to calculate their position coordinates. We obtain the results shown in Table 2, where it can be seen that the ranges of X and Y are both less than 0.02 mm and the repeatability is very good.

5. Comparison and Discussion of Automatic and Manual Testing

The automatic system has been in trial operation for several months. Compared with the experimental data of the manual test system, the actual results show that the system has satisfied expectations in terms of ESD detection, accuracy of test parameters, reliability of the test system, and material consumption during the test. The automatic system effectively guarantees the control of the production environment, reduces the probability of products being polluted by humans, and lays the foundation for product quality. Table 3 shows that the values of the ESD detection data of the system are far less than the company's control requirements, and the data have better reliability. Table 4 shows that the accuracy of the reading and writing position offset of the main parameters of the dynamic performance test is increased by 50%. Table 5 shows that the consumption of test materials by the system is reduced by 60%.

Table 1
Some measured and real values.

Pos num	Robot X	Robot Y	Pixel X	Pixel Y	Target X	Target Y	Cal X	Cal Y	X err (abs)	Y err (abs)
1	−370.0	90.06	247.3	265.6	−320.8	84.08	−320.81	84.093	0.01	0.013
2	−365.5	98.56	530.9	185.7	−320.8	84.08	−320.77	84.144	0.03	0.064
3	−368.0	89.56	277.9	320.6	−320.8	84.08	−320.79	84.092	0.01	0.012
4	−371.5	93.06	282.0	169.8	−320.8	84.08	−320.84	84.142	0.04	0.062
5	−365.5	99.05	541.7	175.3	−320.8	84.08	−320.77	84.152	0.03	0.072
6	−364.5	97.25	523.1	235.5	−320.8	84.08	−320.77	84.129	0.03	0.049
7	−369.5	91.75	295.1	241.4	−320.8	84.08	−320.81	84.127	0.01	0.047
8	−373.5	87.55	118.4	240.7	−320.8	84.08	−320.86	84.041	0.06	0.039
9	−372.3	85.45	97.0	311.5	−320.8	84.08	−320.86	84.017	0.06	0.063
10	−367.9	89.95	288.6	314.6	−320.8	84.08	−320.79	84.013	0.01	0.067
11	−362.6	95.45	523	315.5	−320.8	84.08	−320.76	84.099	0.04	0.019
12	−366.1	93.95	415.8	270	−320.8	84.08	−320.77	84.121	0.03	0.041

Table 2
Results of verifying repeatability of robot positioning.

Target 1	Robot moves 50 times			Target 2	Robot moves 50 times		
	X	*Y*	*U* (degree)		*X*	*Y*	*U* (degree)
1	288.2173	418.9572	132.5432	1	−301.794	406.501	221.8138
2	288.2095	418.9551	132.5468	2	−301.797	406.5	221.8183
3	288.2116	418.9494	132.6005	3	−301.796	406.496	221.8006
4	288.2123	418.9486	132.6004	4	−301.797	406.496	221.8122
5	288.2108	418.9514	132.5403	5	−301.796	406.498	221.8318
6	288.2110	418.9497	132.6021	6	−301.799	406.507	221.8127
7	288.209	418.9529	132.5417	7	−301.797	406.5	221.8143
8	288.2119	418.9548	132.5513	8	−301.798	406.498	221.8226
9	288.2093	418.9529	132.5457	9	−301.797	406.497	221.8064
10	288.2138	418.9463	132.5291	10	−301.799	406.497	221.8205
⋮	⋮	⋮	⋮	⋮	⋮	⋮	⋮
49	288.2046	418.9509	132.5331	49	−301.789	406.498	221.8068
50	288.205	418.9465	132.5182	50	−301.788	406.501	221.7881
Max	288.2173	418.9572	132.6021	Max	−301.787	406.507	221.8593
Min	288.2027	418.9457	132.5159	Min	−301.799	406.493	221.7677
Range	0.0146	0.0115	0.0862	Range	0.0126	0.0138	0.0916

Table 3
ESD testing data.

Detection target	Control item	Company specifications	Test data	Conclusion
Robot auto-test system	Resistance of magnetic head carrier to ground	≤2 Ω	0.4 Ω	Qualified
	Robot resistance to ground	≤2 Ω	0.7 Ω	Qualified
	Packaging tube voltage	≤20 V	3 V	Qualified
	Instant electromotive force	≤500 mv	180 mv	Qualified

Table 4
Reading and writing position offsets.

Test target	Manual (nm)	Automatic (nm)
1	6.27	3.68
2	7.03	1.58
3	8.08	0.81
4	6.27	4.51
5	4.66	1.52
6	14.21	5.13
7	12.18	4.33
8	12.99	4.66
9	13.82	1.86
10	5.99	6.60
Max	14.21	6.60
Min	4.66	1.86
Average	9.14	4.52

Table 5
Number of test magnetic heads per disc.

Day	Automatic (k)	Manual (k)
1	1.8	1.3
2	0.9	1.0
3	5.7	1.2
4	0.8	1.0
5	1.5	1.1
6	1.0	1.1
7	1.6	1.1
8	1.9	1.2
9	3.2	1.0
10	1.3	0.9
⋮	⋮	⋮
29	3.6	0.9
30	2.0	0.8
Average	1.8	1.1

6. Conclusions

In this paper, we presented a design of a dynamic magnetic head test system based on a robot and a CCD image sensor. The system uses piecewise linear transformation to deal with the image of the test target, applies the 3 × 3 median filter method to perform image smoothing, and uses the Robert operator to extract edge features. The design is also based on a constant rotation matrix to simplify the hand–eye calibration of the robot, and high-precision positioning of the target was achieved. The results of system operation show that our design has high practical engineering value, and can greatly improve the test efficiency of magnetic heads, reduce the input cost, and enable strong competitiveness of the enterprise.

Acknowledgments

This work was supported by the Innovative Platform in Industry and Education Integration of Testing Technology for Intelligent Terminal Product (#2020CJPT014) and Research on Intelligent Detection System of FPC Surface Defects Based on Machine Vision (ZXF021), as well as the Electronic Information Technology R & D and service center.

References

1 Z. Sun, D. Zhang, and W. Fang: Sens. Actuators **279** (2018) 284. https://doi.org/10.1016/j.sna.2018.06.014
2 E. G. Stevens, J. A. Clayhold, H. Doan, R. P. Fabinski, J. Hynecek, S. L. Kosman, and C. Parks: Sensors **17** (2017) 2841. https://doi.org/10.3390/s17122841
3 R. Dwivedi, S. Gangwar, S.Saha, V. K. Jaiswal, R. Mehrotra, M. Jewariya, G. Mona, R. Sharma, and P. Sharma: MAPAN **36** (2021) 313. https://doi.org/10.1007/S12647-021-00463-Z
4 P. Astier: J. Instru. **10** (2015) 13. https://iopscience.iop.org/article/10.1088/1748-0221/10/05/C05013
5 K. S. Xia, S. Clint, K. Max, A. Noble, S. Amit, and H. Ramy: Sensors **21** (2021) 1. https://doi.org/10.3390/S21134276
6 P. O. Leary: Comput. Ind. **56** (2005) 997. https://doi.org/10.1016/j.compind.2005.05.023
7 M. Benjamin, D. Mike, C. K. Au. Kit, and S. H. Lim: Comput. Electron. Agric. **189** (2021) 355. https://doi.org/10.1016/J.COMPAG.2021.106355
8 B. Kim, N. Yuvaraj, H. W. Park, K. R. Sri Preethaa, R. A. Pandian, and D. E. Lee: Autom. Constr. **132** (2021) 941. https://doi.org/10.1016/J.AUTCON.2021.103941
9 A. Bouguettayaa, H. Zarzourb, A. M. Taberkita, and A. Kechidaa: Signal Process. **190** (2021) 561. https://doi.org/10.1016/J.SIGPRO.2021.108309
10 E. Chian, W. l. Fang, M. G. Yang, and J. Tian: Autom. Constr. **131** (2021) 100. https://doi.org/10.1016/J.AUTCON.2021.103862
11 M. Hashemzadeh, N. Farajzadeh: Int. J. Comput. Intell. Syst. **9** (2016) 850. https://doi.org/10.1080/18756891.2016.1237185
12 Z. Y. Niu: J. Phys. Conf. Ser. **2006** (2021) 1. https://doi.org/10.1088/1742-6596/2006/1/012008
13 C. Yang: J. Phys. Conf. Ser. **1992** (2021) 1. https://doi.org/10.1088/1742-6596/1992/3/032039
14 M. Eshkevari, M. J. Rezaee, M. Zarinbal, and H. Izadbakhsh: J. Manuf. Process. **68** (2021) 973. https://doi.org/10.1016/J.JMAPRO.2021.06.018
15 A. Naseri and A. R. Nasab: J. Ambient Intell. Hum. Comput. **1** (2021) 1. https://doi.org/10.1007/S12652-021-03474-5
16 Y. Zhang, Z. W. Wang ,Y. H. Wang, C. L. Zhang, and B. Zhao: Front. Phys. **9** (2021) 1. https://doi.org/10.3389/FPHY.2021.701462
17 Q. Fan, Z. Gong, S. Zhang, B. Tao, Z. P. Yin, and H. Ding: Rob. Comput. Integr. Manuf. **68** (2021) 1. https://doi.org/10.1016/j.rcim.2020.102078
18 J. Jin, W. Hao, D. Yang, Z. Tan, and C. Zheng: J. Phys. Conf. Ser. **1939** (2021) 1. https://doi.org/10.1088/1742-6596/1939/1/012027

19 Y. Kwon and J. Hong: Rob. Comput. Integr. Manuf. **30** (2014) 451. https://doi.org/10.1016/j.rcim.2014.02.004
20 T. Li and C. Liu: Optik **173** (2018) 13. https://doi.org/10.1016/j.ijleo.2018.07.103

About the Authors

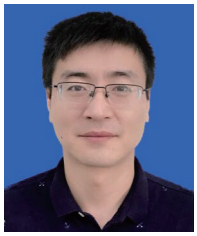

Long Gao received his B.S. degree in measurement and control technology and instrumentation from Southwest Jiaotong University, Chengdu, China, in 2004, and his M.S. degree in testing and measuring technology and instruments from Southwest Jiaotong University, Chengdu, China, in 2007. He is currently teaching in the School of Electronic Information of DongGuan Polytechnic. His research interests include machine vision, pattern recognition, signal processing, and fault diagnosis. (gaol@dgpt.edu.cn)

Jian-Yong Bian received his Ph.D. degree from South China University of Technology. He is currently teaching in the School of Electronic Information of DongGuan Polytechnic. His current research interests include machine vision, pattern recognition, and image processing. (Bianjy@dgpt.edu.cn)

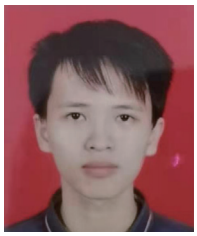

Feng-Peng Wang received his M.S. degree from Huazhong University of Science and Technology, China, in 2009. He is currently working as a testing manager at Xinke Magnetoelectric Co., Ltd., China. His research interests are in testing, robots, and sensors. (39578177@qq.com)